Hindawi
Structural Control and Health Monitoring
Volume 2023, Article ID 2586728, 18 pages
https://doi.org/10.1155/2023/2586728

Research Article

Life Cycle Monitoring of Offshore Steel Pipe Piles via UWFBG Wireless Sensor Network

Jinghong Wu[1], **Shaowen Xu**[1], **Le Qi**[2], **Zhihao Meng**[2] **and Lixiang Jia**[3]

[1]*School of Civil Engineering, Suzhou University of Science and Technology, Suzhou 215011, China*
[2]*Shandong Electric Power Engineering Consulting Institute Co., Ltd., Ji'nan 250013, China*
[3]*Suzhou NanZee Sensing Technology Co., Ltd., Suzhou 215123, China*

Correspondence should be addressed to Jinghong Wu; wjh@mail.usts.edu.cn

Received 28 February 2023; Revised 6 June 2023; Accepted 12 June 2023; Published 24 June 2023

Academic Editor: Chia-Ming Chang

Monitoring the stress and deformation state of offshore steel pipe piles is very necessary for complex ocean environments. However, challenges still remain in remotely capturing detailed data on offshore projects. Herein, an ultraweak fiber Bragg gratings- (UWFBGs-) based wireless sensor network was established to obtain the high-precision strain along the piles. The No. 3 offshore wind power safety monitoring project in South Shandong Peninsula, China, used such a fiber-optic monitoring system. From January 1 to June 1, 2022, strain profiles of three offshore steel pipe piles were measured in seconds with a 1 m spatial resolution and a 1 $\mu\varepsilon$ strain resolution, which clearly show sea level and mud-water interfaces. To assess the pile's operational condition, the displacement and rotational angle of the mud surface are further calculated. It is discovered that the horizontal deformation at sea has a positive correlation with the wind, waves, and current, meanwhile decreasing with depth. The UWFBG-wireless sensor network can realize dynamic monitoring and early warning, which is promising for the life cycle monitoring of offshore wind turbine steel pipe piles.

1. Introduction

In recent years, with the continuous growth of the wind energy market, fewer and fewer wind resources are available for development on the land. Global wind farm construction has shown a trend toward offshore development [1–3]. A steel pipe pile is one of the most common forms of offshore fan foundation, especially a large-diameter ultralong steel pipe pile which has been applied more and more widely [4]. Offshore steel pipe piles are affected by many factors during their working life cycle, including piling, static load, and operation [5]. Their stress and deformation states are complex and directly affect the construction and operation safety of the superstructure. Therefore, it is extremely necessary to monitor the whole life cycle of offshore steel pipe piles [6, 7].

Affected by marine hydrological and meteorological conditions, the construction window period of offshore wind power pile foundations is short and exists in great uncertainty. During the operation period of offshore wind power plants, it is not possible to rely solely on manual on-site inspection, and remote automated testing technology must be used to realize the monitoring [8]. Moreover, the fan foundation with a relatively long pile body is buried in the seawater, as well as the rock and soil mass of the seabed; thus, the environment around has strong corrosion and electrical conductivity [9]. Traditional monitoring techniques like vibrating-string, inclinometer, and resistive sensors require a lot of sensors and signal transmission lines [10]. It is challenging to meet the health monitoring requirements for the entire life cycle of offshore wind power foundations due to issues like poor durability, low survival rate, poor stability, poor real-time performance, and low degree of automation.

Fiber optic sensing has attracted considerable attention in recent years because of its compactness, electromagnetic field immunity, passive operation, multiplexing capacities, chemical stability, biocompatibility, etc. [11]. Different applications of fiber optic sensors have been proposed,

including industry [12], structural health monitoring [13], biochemistry [14], and rehabilitation [11, 15]. This has led to the development of a large number of optical fiber sensors covering physical and chemical parameters for measuring strain [16], temperature [17], pressure [18], pH value [19], and so on. Silica optical fiber (SOF) and plastic optical fiber (POF) are the most concerned and widely used two types of optical fibers [20]. SOF is suitable for long-distance measurement because of its high bandwidth and low attenuation [21], while POF is widely applied to short-distance measurement owing to its large core diameter, good flexibility, lightweight, low elastic modulus, and low cost [22].

Distributed strain sensing technology (DSS) adopts a strain-sensing fiber-optic cable to capture the strain along the entire cable length, which is suitable for long-distance monitoring and can be applied to quantify the infrastructure's deformation [23, 24]. The feasibility of DSS for pile monitoring has been illustrated in previous studies [25–28]. However, most of the DSS techniques can not realize remote transmission and require manual sampling. The fixed and low sampling frequencies are not conducive to exploring the dynamic effect of seawater on the offshore steel pipe pile [29]. Fiber Bragg grating (FBG) technology is attractive for pile foundation structural health monitoring due to its low cost and remote sensing capability [30]. Time-division multiplexing (TDM) technology and wavelength-division multiplexing (WDM) technology are two main multiplexing technologies for expanding the capacity of sensor networks [31]. However, due to signal crosstalk between these normal FBGs, the multiplexing capability is severely limited [32]. In addition, due to a large amount of redundant data in the raster-free area, the system has to adopt the way of low-speed inquiry to obtain the data with higher accuracy, which limits the data observation and makes it impossible to conduct long-distance real-time monitoring of offshore steel pipe piles [33].

UWFBG is a kind of special fiber Bragg grating with very weak reflectivity, usually lower than −20 dB [34]. For this reason, the capacity of Bragg gratings in one fiber-optic cable can be improved to thousands of Bragg gratings [35]. When connecting massive UWFBGs in series, all UWFBGs can be precisely localized based on TDM technology, because the reflection time of the incident light is different for each UWFBG position [36]. UWFBGs effectively increase the sensing distance and multiplexing times of fiber Bragg grating sensors, improves the monitoring accuracy [37], and makes it possible for remote real-time DSS of offshore steel pipe piles.

Herein, a DSS network using UWFBGs was proposed for remote monitoring of offshore steel pipe piles. Such a measurement system was designed detailed and applied to the No. 3 offshore wind power safety monitoring project of the South Shandong Peninsula in China. Along with the offshore static load test, a full-scale measurement of pile strain was conducted by a UWFBG-based sensing system, and the bearing behavior of piles was well analyzed. During the operation period, dynamic and long-term monitoring was carried out for a further understanding of the offshore steel pipe pile working state. This research shows that the UWFBG measurements are the potential for the life cycle monitoring of offshore steel pipe piles.

2. Methodology

2.1. Basic Principle of the UWFBG Technique. FBGs can be obtained by creating periodic variations in the refractive index of the core of an optical fiber. When light is made to pass through the grating, the light reflected by the varying zones of refractive indices will be in phase and amplified at a particular wavelength, which is called the Bragg wavelength. Axial stress and temperature changes are the two factors that will cause the drift of Bragg wavelength, which satisfies the following linear relationship [38]:

$$\frac{\Delta\lambda_B}{\lambda_B} = K_\varepsilon \varepsilon + K_T \Delta T, \tag{1}$$

where $\Delta\lambda_B$ is the change of the FBG central wavelength, ε is the axial strain applied to the optical fiber, ΔT is the temperature change, and K_ε and K_T are the wavelength sensitivity coefficients of strain and temperature, respectively, which can be calibrated in the laboratory. By rearranging equation (1), the axial strain can be obtained:

$$\varepsilon = \frac{1}{K_\varepsilon}\left(\frac{\Delta\lambda_B}{\lambda_B} - K_T \Delta T\right). \tag{2}$$

Benefit from the weak reflectivity, numbers of UWFBGs connected in series with the same refractive index and wavelength ($\lambda_1 = \lambda_2 = \bullet\bullet\bullet = \lambda_n$) can be multiplexed in one fiber core (Figure 1). The received wavelength shifts are used to interpret the strain changes and the reflected time (equation (3)) is used to localize the sensing points [39]:

$$t = \frac{2n_{\text{eff}}d}{c}, \tag{3}$$

where t is the time interval between receiving two UWFBG wavelengths in the fiber, c is the light velocity in the fiber optic, d is the interval distance of UWFBGs, and n_{eff} is the effective refractive index.

2.2. Pile Stress and Force Calculation Based on UWFBGs. The test pile can be divided into a series of monitoring elements because of the small sampling intervals of the UWFBG-based sensing system. As long as the pile is installed with sensing cables correctly, the strain distribution of the pile can be calculated using equation (2) based on the measured Bragg wavelength shifts, and the steel pipe pile axial force F_i can be further calculated [40]:

$$F_i = \overline{\varepsilon}_i E A_i, \tag{4}$$

where F_i denotes the axial force of the steel pipe pile with section i, $\overline{\varepsilon}_i$ is the average strain of section i, E is the elastic modulus of the pile, and A_i is the section area of section i.

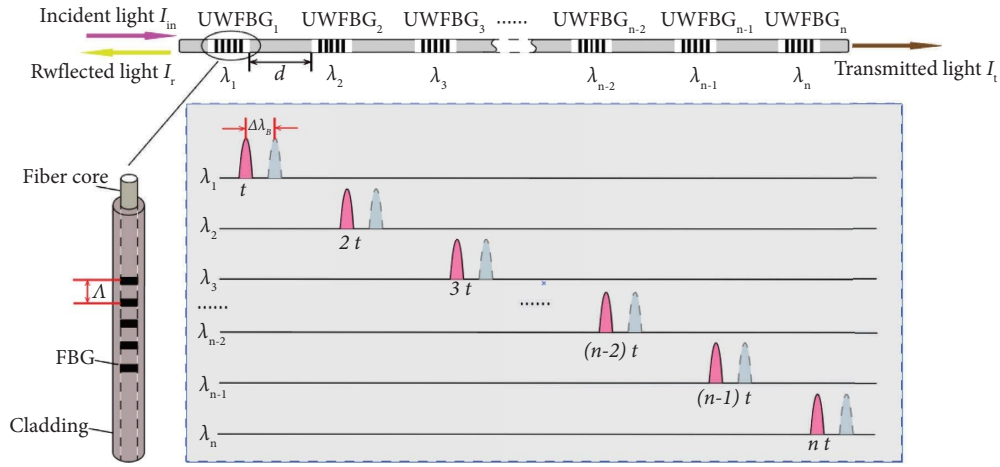

Figure 1: Monitoring principle of UWFBG array.

The vertical loads along the pile propagate downward, and the compression of the upper soil layer will cause reverse shaft friction resistance. According to equations (5) and (6), shaft friction resistance R_i and pile tip resistance R_b of the steel pile can be obtained:

$$R_i = \frac{F_{i+1} - F_i}{\pi u l_i}, \tag{5}$$

$$R_b = \frac{F_b}{A_0}, \tag{6}$$

where l_i denotes the length between section i and section $i+1$, u denotes the outer perimeter, F_i denotes the pile tip axial force, and A_0 denotes the pile end area of the steel pipe pile.

Meanwhile, the pile compression S_s and tip-settlement S_b can be expressed as follows:

$$S_s = \sum_{i=1}^{n} \int_{l_i}^{l_{i+1}} \overline{\varepsilon_i} \cdot \mathrm{d}h, \tag{7}$$

$$S_b = S - S_s, \tag{8}$$

where S is the top settlement of the pile, which can be measured by a dial indicator installed on the top of the pile.

When under horizontal load, the steel pipe pile can be simplified as a fixed cantilever beam structure. The strain values ε_1 and ε_2 captured at the symmetrical position of the pile at the buried depth z, respectively, can be used to calculate the bending strain value ε_m (z). Note that for the strain values, positive represents tension, while negative represents compression:

$$\varepsilon_m(z) = \frac{(\varepsilon_1 - \varepsilon_2)}{2}. \tag{9}$$

Then, the rotational angle θ (z), horizontal displacement ω (z), and bending moment M (z) of the pile can be calculated using the following equations:

$$\theta(z) = \int \frac{\varepsilon_m(z)}{y(z)} \mathrm{d}z + C_1, \tag{10}$$

$$\omega(z) = \int \left[\int \frac{\varepsilon_m(z)}{y(z)} \mathrm{d}z \right] \mathrm{d}z + C_1 x + C_2, \tag{11}$$

$$M(z) = -EI\omega'' = EI\frac{\varepsilon_m(z)}{y(z)}, \tag{12}$$

where I denotes the moment of inertia of the pile section and C_1 and C_2 are the boundary conditions to be calculated. Under simplified conditions, the boundary conditions of steel pipe piles are $z = 0$, $\omega = 0$; $z = 0$, and $\omega' = \theta = 0$. Then, the calculated $C_1 = C_2 = 0$.

2.3. UWFBG Cable and Its Installation. The FO cable with UWFBGs used in offshore steel pipe pile monitoring is the NZS-DDS-C03 cable produced by Suzhou NanZee Sensing Ltd., China, and its mechanical properties are provided in Table 1. The structure of the cable is shown in Figure 2. From inside to outside, the loose-buffered cable consists of a silica FO, UWFBG, buffer, metal-clad pipe, and polyurethane (PE) jacket. This FO cable adopts a unique internal fixed point design, which can realize the distributed measurement of discontinuous and nonuniform strain. The manufactured UWFBG cable is identically spaced to the 1 m UWFBG array.

Before the field investigation, the reproducibility and repeatability of the UWFBG cable need to be verified. As shown in Figure 3, a 1 m long FO cable with a UWFBG cutting from the same UWFBG cable is glued with an interval of 1 m and horizontally fixed at the performance test instrument with a length of 1 m. Such a strain-based performance test instrument can extend the cable by using the motor with a certain velocity. During the tensile process, the displacement is increased from 0 mm to 10 mm with a gradient of 1 mm. Then, the cable rebounds to the initial length with a gradient of −2 mm. The NZS-QDS-A01

Table 1: Mechanical properties of the NZS-DDS-C03 cable.

Number of fiber cores	Grating center wavelength (nm)	Reflection rate (%)	Strain test range ($\mu\varepsilon$)	Cable diameter (mm)	Fiber diameter (μm)	Fixed point spacing (m)
1	1527~1568	0.01	15000	2.5	0.9	1

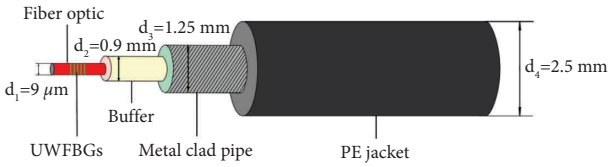

Figure 2: Structure of the NZS-DDS-C03 fiber optic cable.

UWFBGs interrogator analyzes the wavelength results after each displacement, and its technical specifications are summarized in Table 2. The same procedure is repeated five times. Figure 4(a) shows that both the tensile and rebound curves have a good linear relationship, with the tensile and rebound paths basically overlapping. There is no great fluctuation between the five tests, proving a good reproducibility and repeatability of the cable. Finally, the strain coefficient of this cable is calibrated to be 847.03 $\mu\varepsilon$/nm, which is calculated by equation (2).

In addition, to verify the stability of strain monitoring in a long-term state, the cable is stretched to 5 mm, at which point the cable achieves a strain of 5000 $\mu\varepsilon$. Then, the stretch is kept, and the wavelength values are recorded at one-hour intervals for 11 hours, with five sets of data recorded at a time. As it is shown here, the strain differences are basically within $\pm 5\,\mu\varepsilon$ during 11 h, illustrating the stability of long-term monitoring (Figure 4(b)).

In the field, the UWFBG cable is implanted into carbon fiber cloth to form carbon fiber composite optical cables, which are symmetrically arranged on the inner side wall of piles in a U-shape (Figure 5). After basic cleaning such as line fixing, grinding, and dust removal, fixed-point laying is carried out; that is, the sensing cable is laid on the grinding surface, fixed with strong glue, and fully pasted with epoxy adhesive along the laying line (Figure 6(a)). After the adhesive curing strength reaches more than 50%, gold foil paper is pasted on the surface to prevent later welding slag from burning (Figure 6(b)). A section of channel steel is welded at the bottom of the pile to prevent the cable from being damaged during piling (Figure 6(c)). At the top of the pile, the cable lead is protected with the steel hose and passed through the inner platform with a hoop fixed on the hook to prevent the line from falling off. The sensing cable then is integrated into the main optical cable (Figure 6(d)) and connected to the reserved interface of the fan ring network. It is transmitted to the booster station through the fan ring network and then connected to the monitoring equipment (Figure 6(e)). Finally, equipment demodulation control software and monitoring software are installed in the onshore centralized control center to realize real-time online monitoring of the pile foundation.

It is important to point out that additional temperature compensation is necessary and important in areas where seawater temperature variations are strongly influenced by solar radiation and climate change.

2.4. UWFBG Sensor Network for Offshore Steel Pipe Piles. As shown in Figure 7, for offshore steel pipe pile monitoring, a UWFBG- wireless sensor network is established. Working as the sensing module, the sensing cables with UWFBGs for pile monitoring are tested indoors first and then installed correctly to the steel pipe pile (Figures 7(a) and 7(b)). Then, the wavelength is interpreted in time by using the UWFBG interrogator and remotely transmitted to the onshore centralized control center via 4G/5G Internet in the transmission module within 10 s (Figure 7(c)). Subsequently, the strain profile along the entire pile is output, and the target results are calculated according to the user requirement, mainly the pile force and the pile displacement (Figure 7(d)). Finally, a suitable warning algorithm is integrated into the early warning module to analyze the critical state of the offshore steel pipe pile and decides whether to warn or not.

3. Offshore Static Load Tests

3.1. Test Plan. Before the actual application, static load tests were carried out to verify the feasibility of the system. The anchored pile reaction method was used in the static load test. As shown in Figure 8(a), the test apparatus mainly consisted of anchored piles, reaction beams, base beams, and hydraulic jacks. The hydraulic jacks exerted the load on the pile top through the reaction force provided by reaction beams and four anchored piles. The settlement of the pile top was obtained by the dial gauges arranged around the top pile body. The static load test plan referred to the code (JTS237-4-2017). Each load stage was applied for 1 hour, and the load was from the initial value of 6000 kN to a maximum of 39000 kN with a gradient of 3000 kN for the first 7 stages and 1500 kN for the rest. The unloading process was maintained for 15 min for every stage with a gradient of 6000 kN. After complete unloading, the system was maintained for 1 hour.

No less than 2 days after the vertical static load test, the horizontal static load test was carried out (Figure 8(b)). The unidirectional single cycle-loading method was adopted, and the static load test plan referred to the code (JTS237-4-2017). Each load stage was applied for 1 hour, and the load was from the initial value of 100 kN to a maximum of 1000 kN with a gradient of 100 kN for the first 4 stages and 50 kN for the rest. The unloading process was maintained for 10 min for every stage with a gradient of 200 kN. After complete unloading, the system was maintained for 30 min.

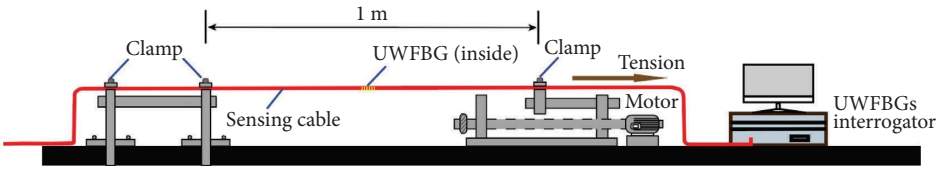

Figure 3: Diagram of the strain-based performance test instrument for the UWFBG cable.

Table 2: Technical specifications of the NZS-QDS-A01 UWFBGs interrogator.

Operation wavelength (nm)	Channels	UWFBGs/channel	Resolution (pm)	Spatial resolution (m)	Measurement length (km)	Sampling time (min)
1525–1565	16	>2000	1	≥0.5	≤20	≤1

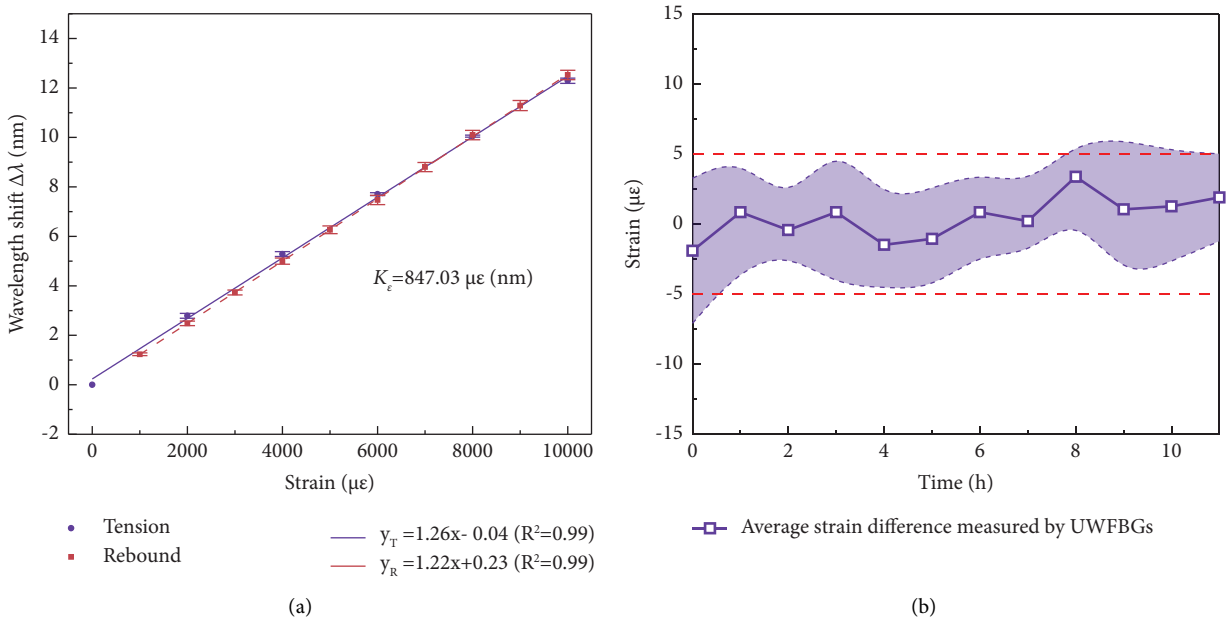

Figure 4: Performance tests results of the (a) tensile-rebound test and calibration and (b) stability test.

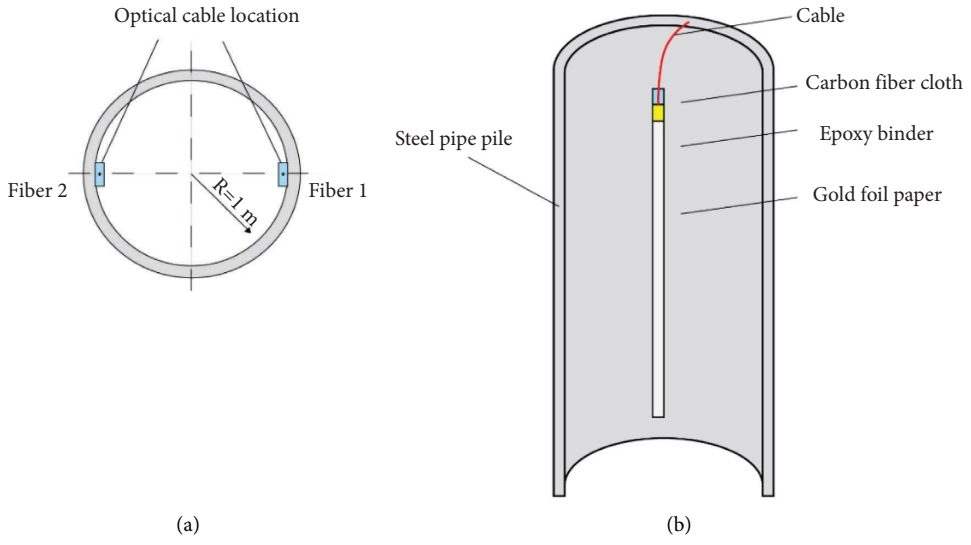

Figure 5: Schematic diagram of optical cable layout: (a) top view and (b) sectional view.

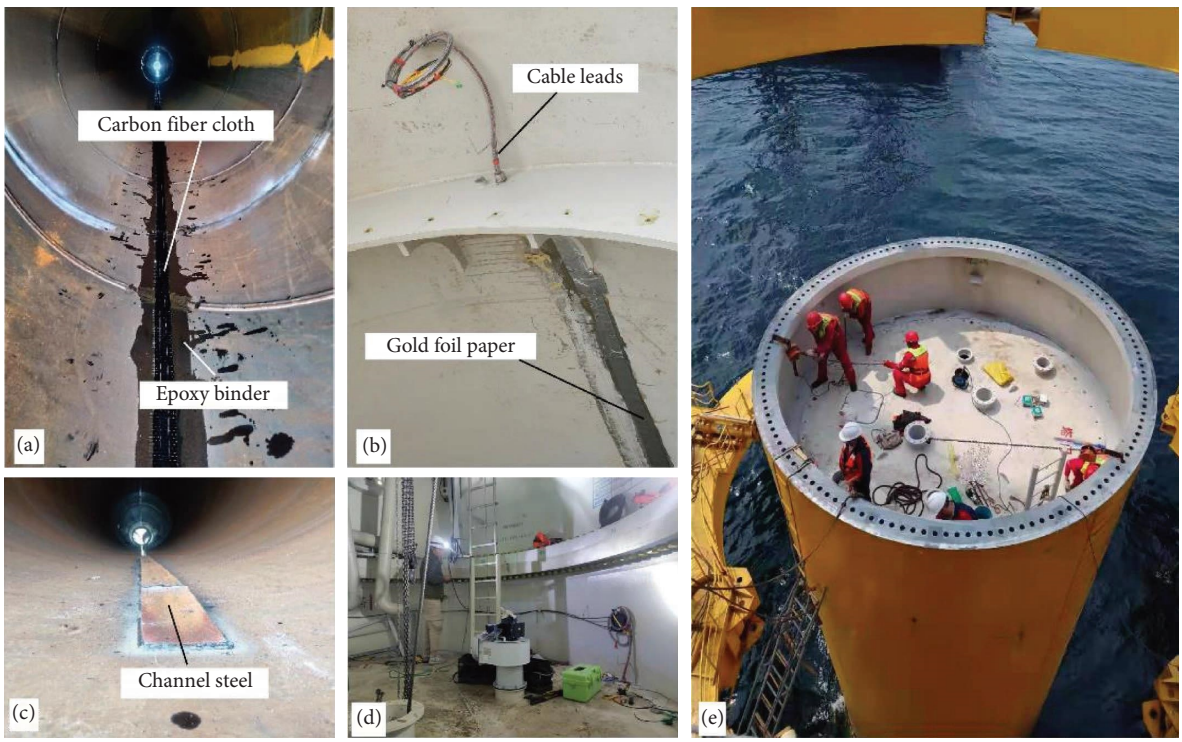

FIGURE 6: Installation of FO cables for offshore steel pipe piles: (a) the adhesive of the optical cable; (b) protection of cable leads; (c) channel steel welding protection at pile bottom; (d) cable integration; (e) monitoring station.

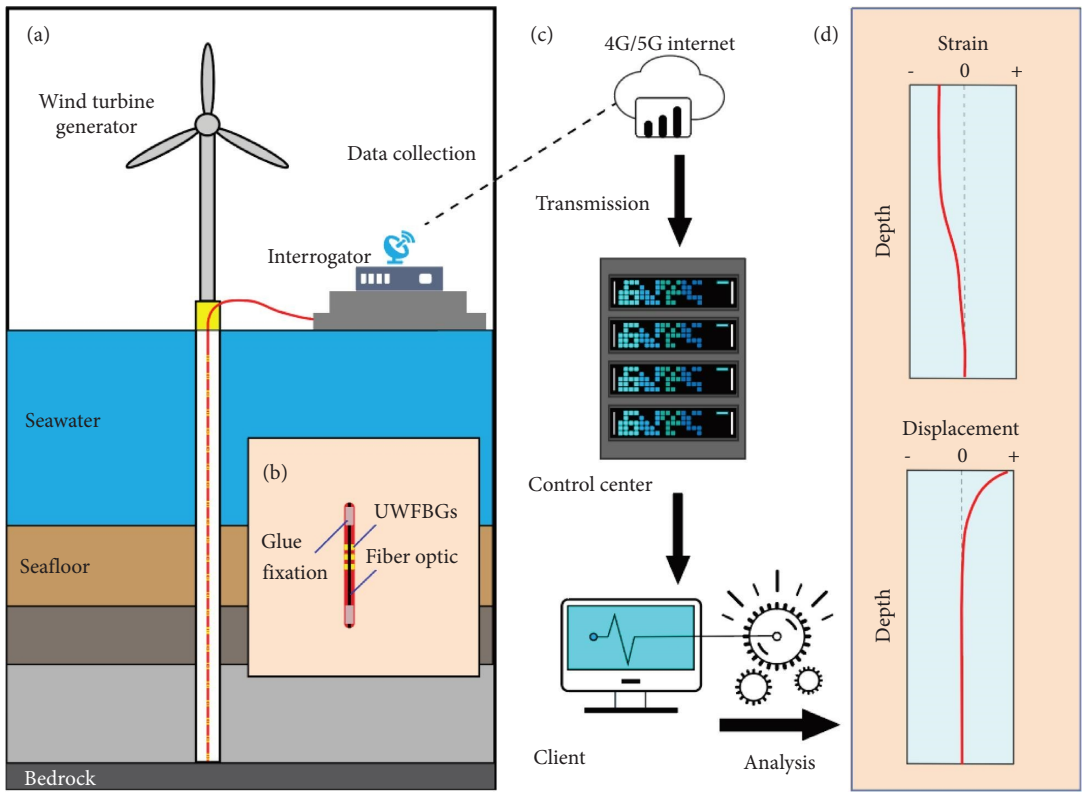

FIGURE 7: UWFBG-wireless sensor network for offshore steel pipe pile monitoring.

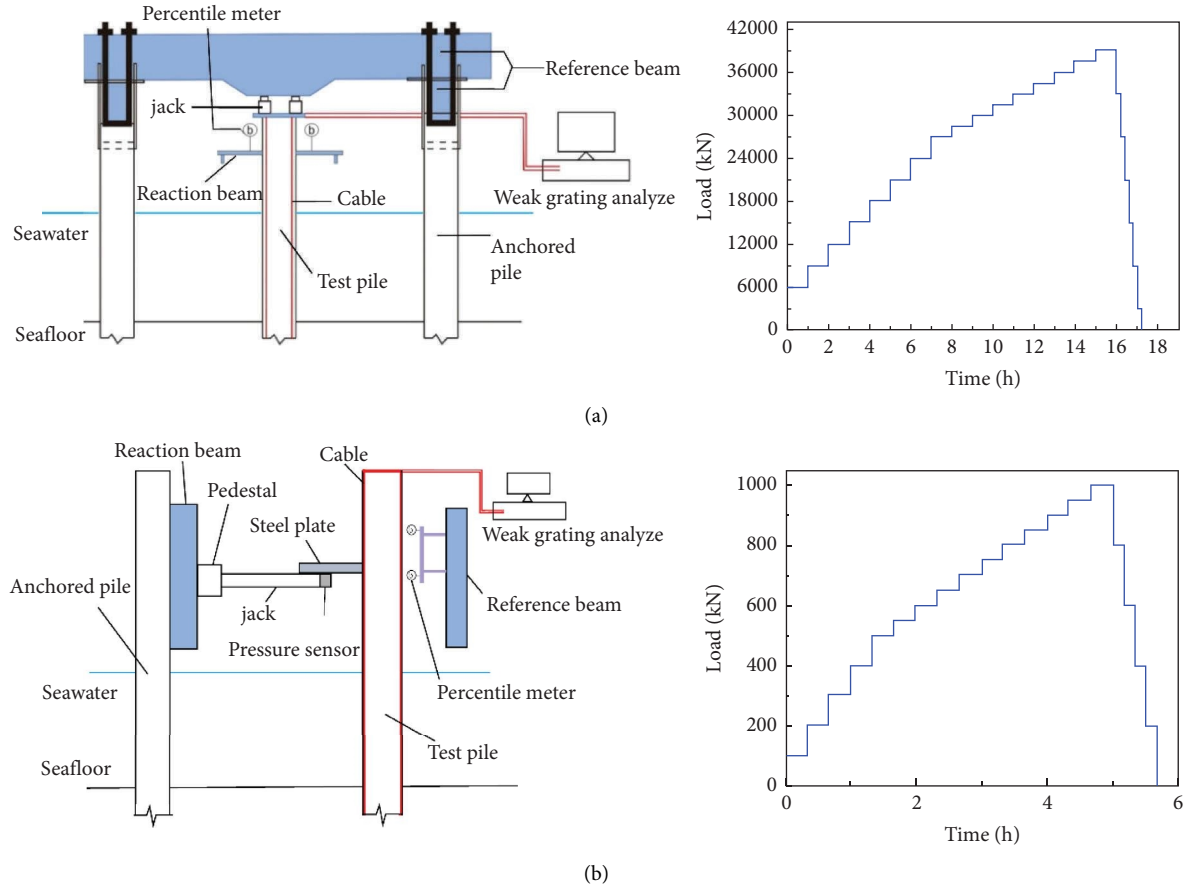

FIGURE 8: Offshore static load tests: (a) test apparatus and test schedule of the vertical test and (b) test apparatus and test schedule of the horizontal test.

The FO cables with UWFBGs were connected to the instrument, and the initial Bragg wavelength shift along the cable was measured by using the UWFBGs interrogator before the static load test. During the static load test, the drift of Bragg wavelength under each load will be measured until the end of the test. According to equation (2), the strain distribution of the cables under each load can be obtained.

3.2. Vertical Static Load Test. The manufactured UWFBG cable is identically spaced to the 1m UWFBG array; as a result, the strain can be obtained every 1 m along the pile depth under each load (Figure 9(a)). It can be seen that the strain of the UWFBG cable increased steadily with an increase in the load and decreased with an increase in the buried depth of the pile body (Figure 9(a)). The strain distribution along the pile can be divided into four parts: a transition zone existed at the pile head. In the seawater, the strain was quite uniform, and in the soil part, the strain decreases gradually with the depth of the pile due to the effect of the shaft friction. The rate of strain decline was different due to different friction resistance and pressure load. It was noted that, at the depth of about −45 m, the thickness of the steel pipe pile changed from 30 mm to 24 mm, which led to a sudden increase in pile strain and then continued to decrease with the increase in depth.

Young's modulus E is 206 GPa and the cross-sectional area A is 0.07–0.09 m^2 which are all fixed values in this case. Pile axial force and shaft friction under each load were calculated by equations (4) and (5), and the distribution of the axial force is shown in Figure 9(b). The shaft friction was further averaged for each soil layer according to the soil layer distribution as shown in Figure 9(c). The downward transfer load of the pile decreased continuously with an increase in depth due to the shaft friction. Figure 9(c) shows that the peak value of shaft friction was between a depth of −74.5~−75.5 m, which was located in dense Layer 5. This was mainly caused by the different densities of soil layers.

The development of shaft friction in different soil layers and tip resistance with top loads are plotted in Figure 10. It indicated that the top load was shared by the shaft friction and tip resistance. The tip resistance increased linearly with an increase in the load. The shaft friction bored most of the top load, while the tip resistance only bored 16.89% of the top load under the maximum load. This test pile should be defined as an end-bearing friction pile. The slope of the shaft friction curves of Layers 2, 3, and 4 gradually slowed down, indicating that the shaft friction of these soil layers was about to be fully realized. While the shaft friction of Layer 5 was still increasing, that is, there was still a certain space from the recommended values of the geotechnical investigation report.

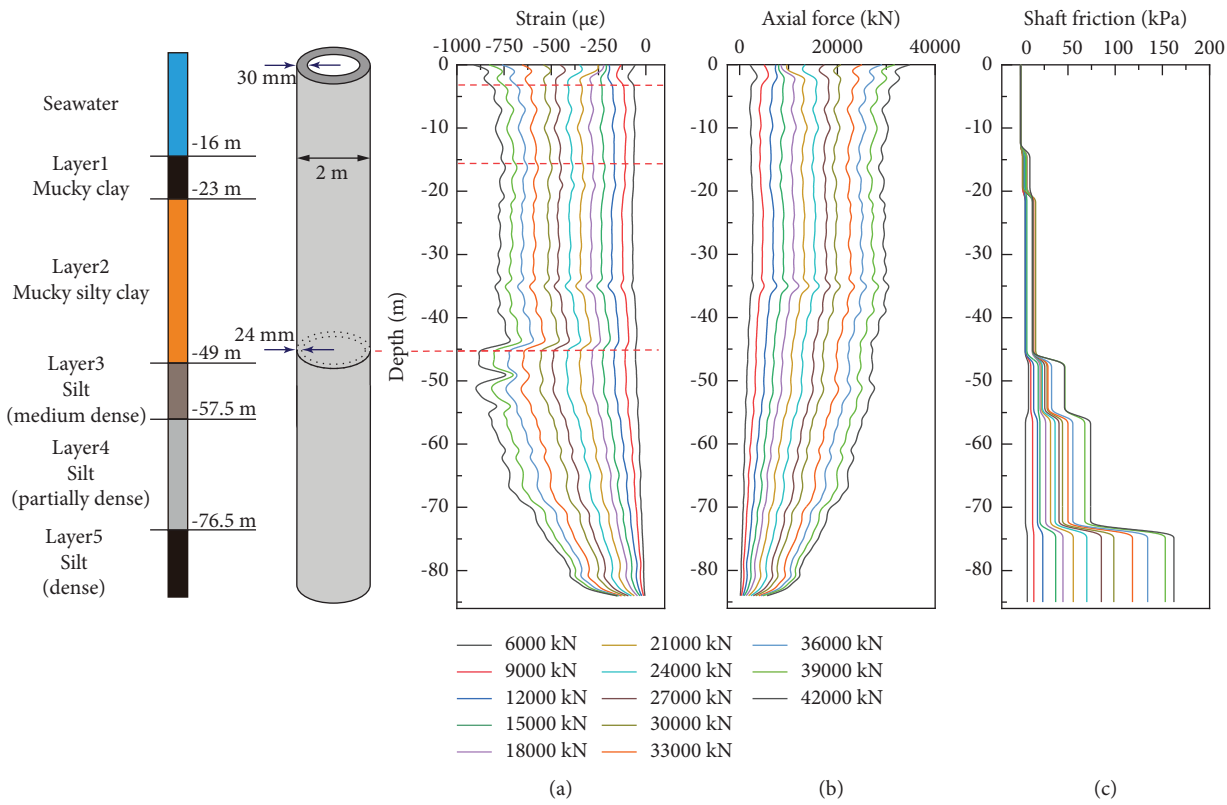

Figure 9: Curves of strain distribution of pile (a), axial force (b), and (c) shaft friction.

The pile compression S_s and tip-settlement S_b calculated according to equations (7) and (8) and the top settlement monitored by the dial gauges are shown in Figure 11. As the load increased, the pile compression, tip-settlement, and top settlement both gradually increased. The top settlement was borne by the compression of the pile and the settlement of the pile end, most of which was pile compression. When the load increased to 37500 kN, the pile compression began to ease and the settlement of the pile tip came into play. In addition, it could be seen that the steel pipe pile had not reached the ultimate bearing capacity.

3.3. Horizontal Static Load Test. As shown in Figure 12, the distributed strain of F1 and F2 was in an antisymmetric relationship under the horizontal force, acting in the connection direction of F1 (Fiber 1) and F2 (Fiber 2). The results indicated that the F1 side was subjected to tensile stress; oppositely, the F2 side was subjected to compressive stress. The strain of the steel pipe pile increased with an increase in horizontal load and reached the maximum value of 1304 $\mu\varepsilon$ at a load of 1000 kPa, and the position was at −26 m. The strain increased first with an increase in the depth, reached maximum approximately at −22 m to −26 m, and then began to decrease. From −53 m to −85 m, the strain remained unchanged with the load and was approximately around 0 $\mu\varepsilon$. The strain at F2 was antisymmetric with F1, showing good consistency of monitoring and indicating that the stability of the pile-bearing capacity was not lost under different horizontal loads.

The bending moment was calculated by equation (12), and the distributed displacement cure of the pile was obtained by the second integral of the corresponding curve which is shown in Figure 13. The bending moment of the pile body was mainly distributed in the range of about 40 m below sea level. With an increase in depth, the bending moment increased first and then decreased. The maximum bending moment point was between Layer 1 and Layer 2 and gradually transferred to deeper. That was because the pile had a flexural deformation under the horizontal load. With an increase in horizontal load, the yield zone of soil around the pile gradually expanded downward, and the maximum bending moment of the pile also shifted to the lower part due to the decrease of the resistance of the upper soil. As the load increased, the absolute value of the displacement measured by the UWFBG increased. The maximum displacement occurred at the uppermost end of the fiber and generated under the 1000 kN load was 544 mm. The horizontal displacement gradually decreased along the pile depth and was almost no longer affected by the horizontal thrust beneath a depth of −30 m.

During loading, the horizontal displacement was also measured by using the dial indicators, as shown in Figure 14. The two values were consistent before 600 kN, the monitored value was slightly smaller than the measured value after 600 kN due to the deformation coordination of the pile, and the sensing cable became worse under large deformation. The maximal absolute error was 75 mm, and the average value was 16 mm. The relative error was further analyzed by the MAPE (mean absolute percentage error) method [41] to

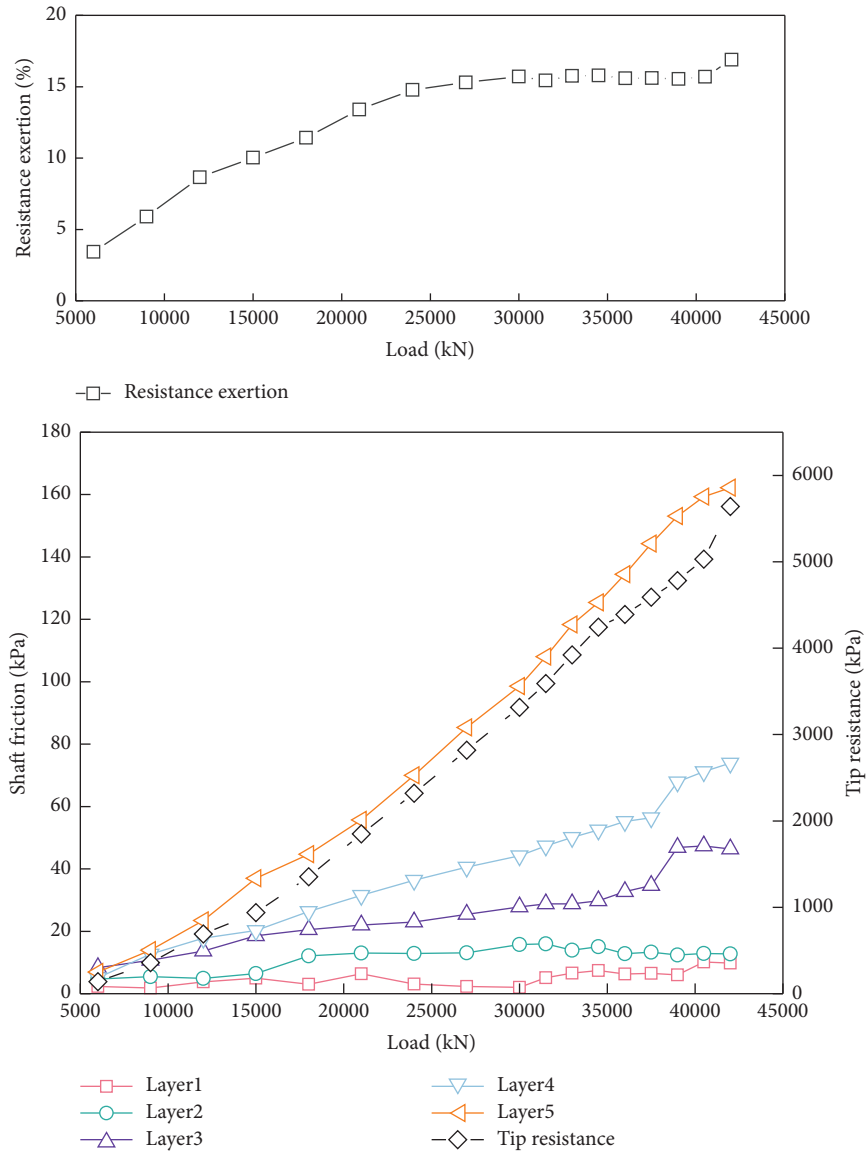

FIGURE 10: Development of shaft friction and tip resistance of the pile with loads.

verify the accuracy of displacement calculated by the UWFBGs. MAPE can be calculated by the following equation:

$$\text{MAPE} = \frac{1}{n}\sum_{t=1}^{n}\frac{|y_t - \hat{y}_t|}{y_t}, \tag{13}$$

where y_t denotes the true value as a comparison, $\hat{y}_t$ denotes the value to be compared, and n denotes the sample capacity.

After calculation, the MAPE value, in this case, was 0.058, which showed that the full-scale distributed displacement data calculated by UWFBGs were relatively accurate and credible.

4. Offshore Steel Pipe Pile Monitoring in the Shandong Peninsula

4.1. Overview of the Study Area. The FO wireless sensor network was deployed to the No. 3 offshore wind project in South Shandong Peninsula, China (Figure 15). Yellow Sea circulation is the main current in the study area. It is basically composed of the Yellow Sea warm current, carrying high temperature and high salt water northward, and two east-west coastal currents along its two sides, which migrates southward [42]. This coast has relatively strong tides and weak waves with an average one-tenth large wave height $H_{1/10}$ of 0.7 m, an average cycle of 4.6 s, and an average tidal range of 2.78 m

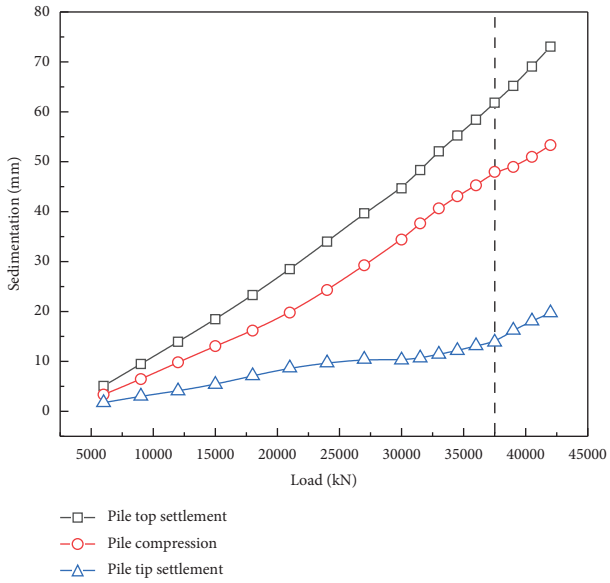

Figure 11: Development of vertical displacements of the pile with loads.

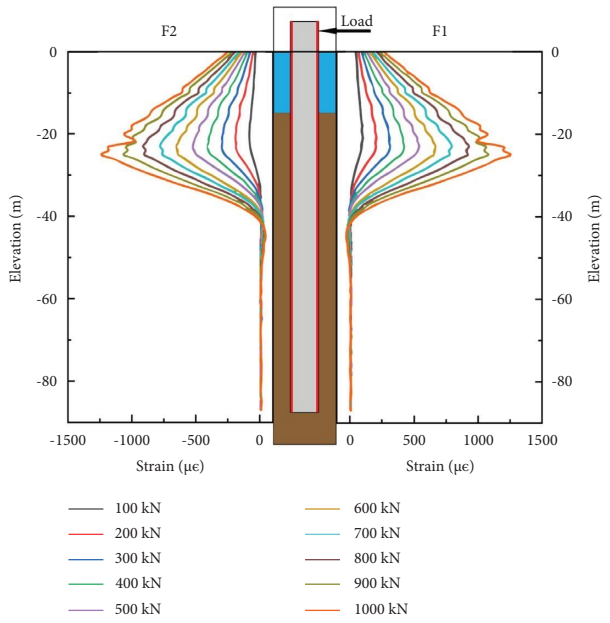

Figure 12: Strain values of the corresponding elevation from 100 kN to 1000 kN.

[43]. The seawater depth is shallow in this sea area, with a depth of 0–50 m.

The first phase of the wind farm was planned to install 58 wind power units (A01~A58) with a single-pile steel pipe pile foundation. The steel pile had a length of 97 m, a pile diameter of 1 m, and a wall thickness of 24–30 mm. A 220 kV offshore booster station and an onshore centralized control center were together constructed (Figure 15(c)). Three wind power piles A14, A41, and A45 were selected for operation period monitoring. After completing the integration of single pile lines of three steel pipe piles, the single pile lines were connected to the corresponding monitoring interfaces. Line integration of equipment access and monitoring signal output was completed at the booster station to ensure smooth transmission of monitoring data to the onshore central control center. Three offshore steel pipe piles had been monitored in real-time during operation. Since January 1, 2022, the monitoring frequency could be set according to the demand, even up to the second level.

As for offshore pile foundation monitoring, the wavelength variation due to pile strain is much greater than the effect of temperature. However, the seawater levels can fluctuate frequently due to tidal action, with fluctuations within a range of 3 m in the study area which may lead to anomalies in both tensile and compressive strains on the same side of the pile. Thus, only the data 3 m below sea level were used for further analysis. Moreover, according to the China Argo Real-time Data Center, the distribution curve of seawater temperature along the depth is approximately a straight line, showing basically no change in the 0–50 m depth of this area. That is, the effect of temperature is relatively small, so no additional temperature compensation was made in this case.

4.2. Long-Term Monitoring Results during the Operation Period. The real-time monitoring data of the A41 wind power foundation were selected at 00:00 time every day from January 1, 2022, to June 1, 2022, to obtain the strain distribution curves of the symmetrical sensing cable on both sides of the pile. As shown in Figure 16, the strain curve reflected the sea level and mud-water interface. In seawater, the pile strain gradually decreased with the increasing depth and presented a stable distribution near the seabed mud surface. After entering the soil layer, the strain value gradually decreased with the depth, but the pile bottom was not affected. The maximum strain of the pile under a sea level occurred near the sea surface, which was about 250 $\mu\varepsilon$. During the operation of the wind turbine, the wind and waves at sea will produce horizontal loads on the pile foundation. According to the symmetrical cable strain, one side of the pile exhibits tensile strain and the other side exhibited compressive strain, and the strain values were the same. The horizontal displacements calculated by equation (11) are shown in Figure 17, the results indicated that the maximum displacement occurred at the uppermost end of the fiber, and the absolute value was 58 mm. There was no horizontal displacement of the pile from the pile bottom to −50 m elevation; that is, under the existing horizontal load, the pile was completely constrained after it is about 18 m into the soil.

4.3. Influence Factors of Offshore Steel Pipe Pile Structure Health. The offshore wind turbine pile foundation is built in a complex marine environment and subjected to the combined action of long-time wind, wave, current, and other dynamic loads, which leads to the deviation and bending of the fan foundation, and even causes a series of safety problems such as deformation, liquefaction, and instability

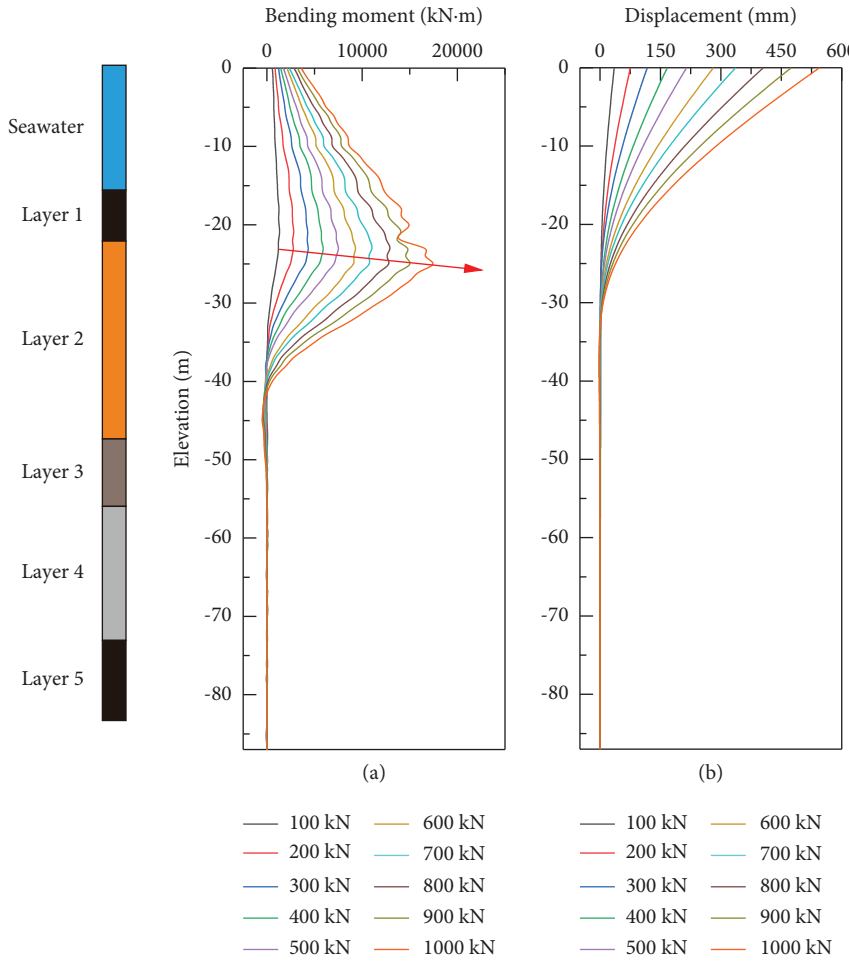

Figure 13: Curves of bending moment (a) and horizontal displacement (b) of F1.

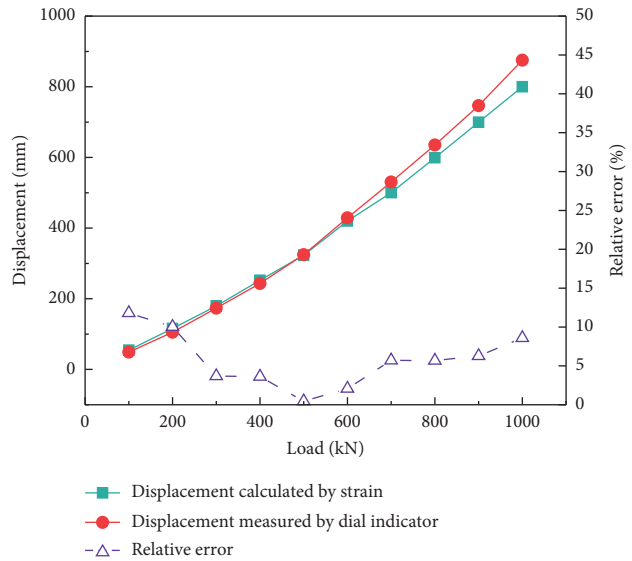

Figure 14: The error between the monitored value of UWFBG and the actual measured value.

of the seabed around the fan pile foundation. The wind load is an important load acting on the fan blades and tower cylinder, which will produce huge horizontal thrust and overturning moment, and causes the horizontal swing of the pile body. In addition, the wave is always accompanied by water flow in the process of propagation, and the wave flow

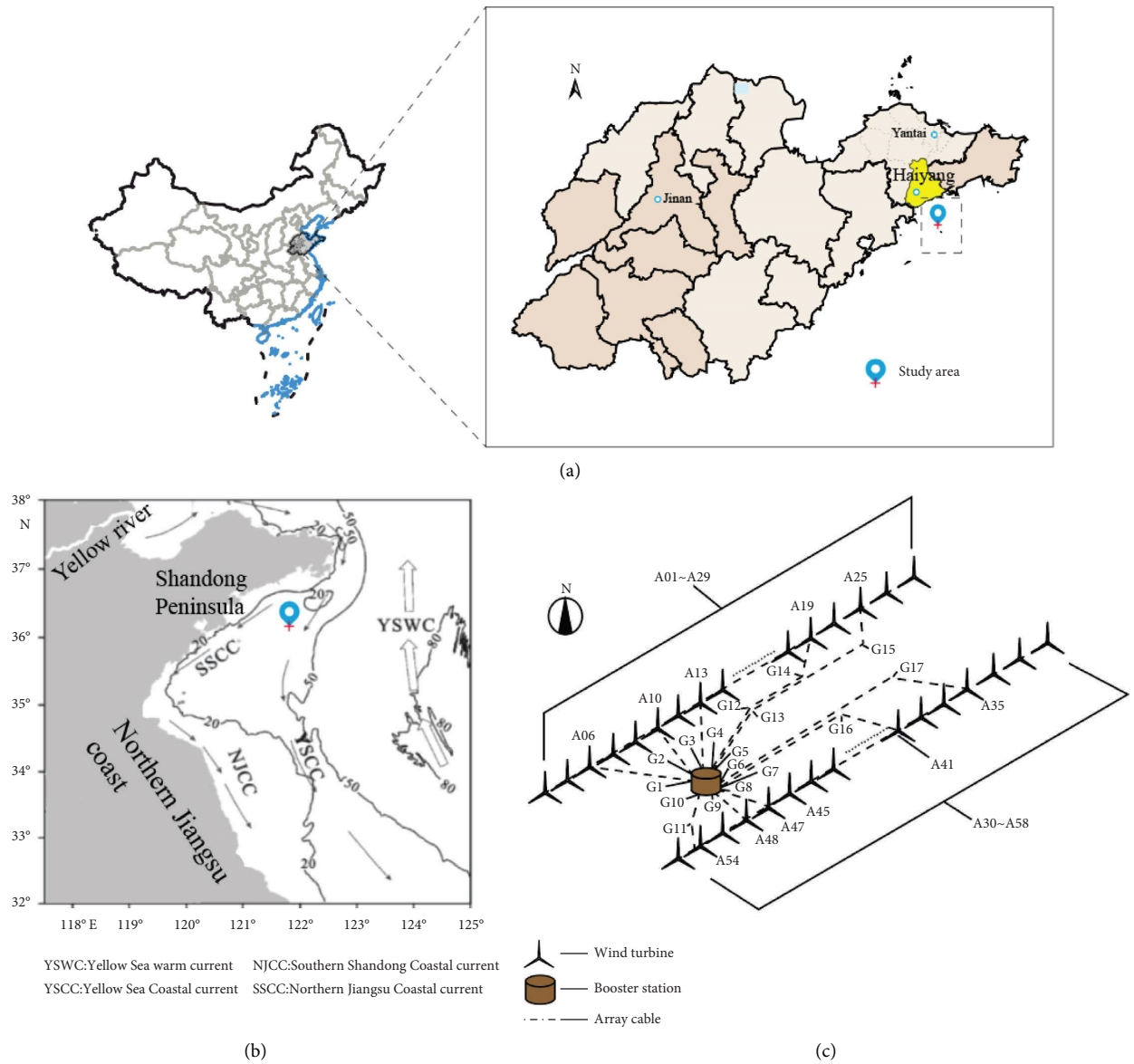

FIGURE 15: Overview of the study area: (a) the location of the study area; (b) current distribution in the South Yellow Sea during winter; (c) the layout map of the wind farm.

load will produce a horizontal cyclic load on the foundation of the offshore fan pile, resulting in horizontal displacement. At the same time, the wave load acting on the sea bed will generate vertical cyclic load on the sea bed surface in the process of continuous propagation and transfer to the pile foundation to generate additional horizontal displacement.

Figure 18 shows the variation curve of the pile mud surface angle calculated according to equation (10) under different wind speeds and wave heights from January 1 to January 29. It can be found that pile swing amplitude had a significant correlation with wind speed and wave height. The increase in wind speed led to the increase of horizontal thrust and overturning moment of the pile foundation; meanwhile, the larger wind speed led to the acceleration of wave velocity, which increased the wave height, aggravated the wave disturbance around the pile, and intensified the angle of the pile mud surface.

To further analyze the swing characteristics of the pile under working conditions, the variation curves of pile strain at different depths of the pile foundation from 18:00 to 18:10 on January 1 are shown in Figure 19(a). It can be seen that the steel pipe pile presented a state of horizontal swing. The oscillation amplitude was the most obvious at the sea surface and became smaller with increasing depth. There was no oscillation at the bottom of the pile foundation. The variation curves of the pile strain at a depth of −2.4 m from 18:00 to 18:10 on the first day of each month in the monitoring cycle in Figure 19(b) show that the swing amplitude of the

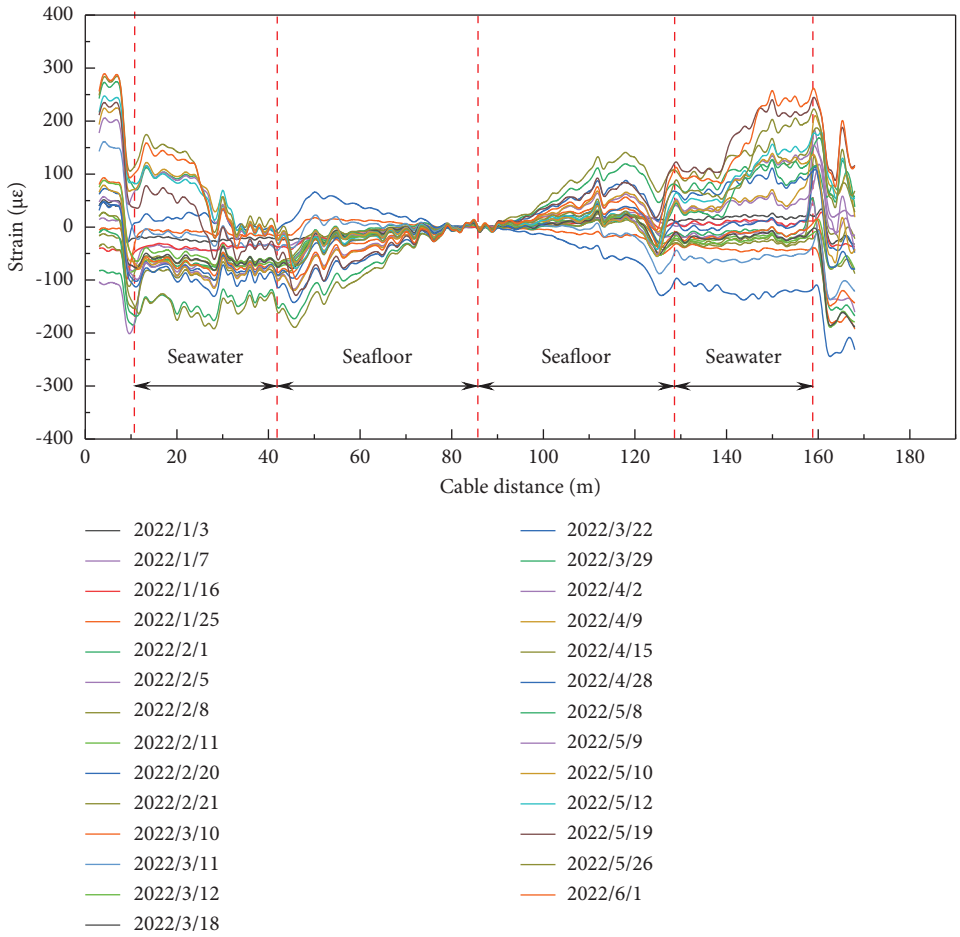

Figure 16: Strain distribution of A41 pile.

pile also presented a certain correlation with the seasonal ocean current. In the winter of January and February, the ocean current movement was strong, the velocity was fast, and the wind and waves were large; hence, the amplitude of the pile foundation swing was also severe. In spring and summer from March to June, the movement of ocean currents was weak, so the amplitude of the pile foundation swing was relatively gentle.

4.4. Working State Evaluation and Early Warning. According to the DNV-OS-J103 specification [44], offshore wind turbine single pile foundations can be divided into four limit states, which are ultimate limit state (ULS), fatigue limit state (FLS), accidental limit state (ALS), and serviceability limit state (SLS). Previous research has shown that the failure of the foundation is mainly caused by piles exceeding the allowable rotation angle under the SLS [45]. The wind, wave, and current loads applied to the offshore wind turbine are not constant static but long-term cyclic forces. During the service of the wind turbine, the cycle loads of the foundation can reach 10^7~10^8 times. Under the cyclic load, the soil stiffness around the foundation is constantly weakened and the plastic strain accumulates, which eventually leads to excessive lateral displacement at the mud surface of the pile foundation, thus resulting in SLS failure. DNV-ST-0126 [46] specifies that the rotational angle of the mud surface caused by the cyclic load should not exceed 0.25° for a single-pile offshore fan foundation.

The FO wireless sensor network previously proposed is recommended for working state evaluation and early warning for the wind turbine foundation infrastructure. First, real-time monitoring of pile strains is realized by UWFBG technology. Then, the spatialtemporal data are transmitted to the cloud module and server for processing by the transmission module and 4G/5G Internet to calculate the rotational angle of the pile at the corresponding time. Here, we set 0.25° as the serviceability limit safety threshold. Once the rotation angle at the mud surface exceeds the safety

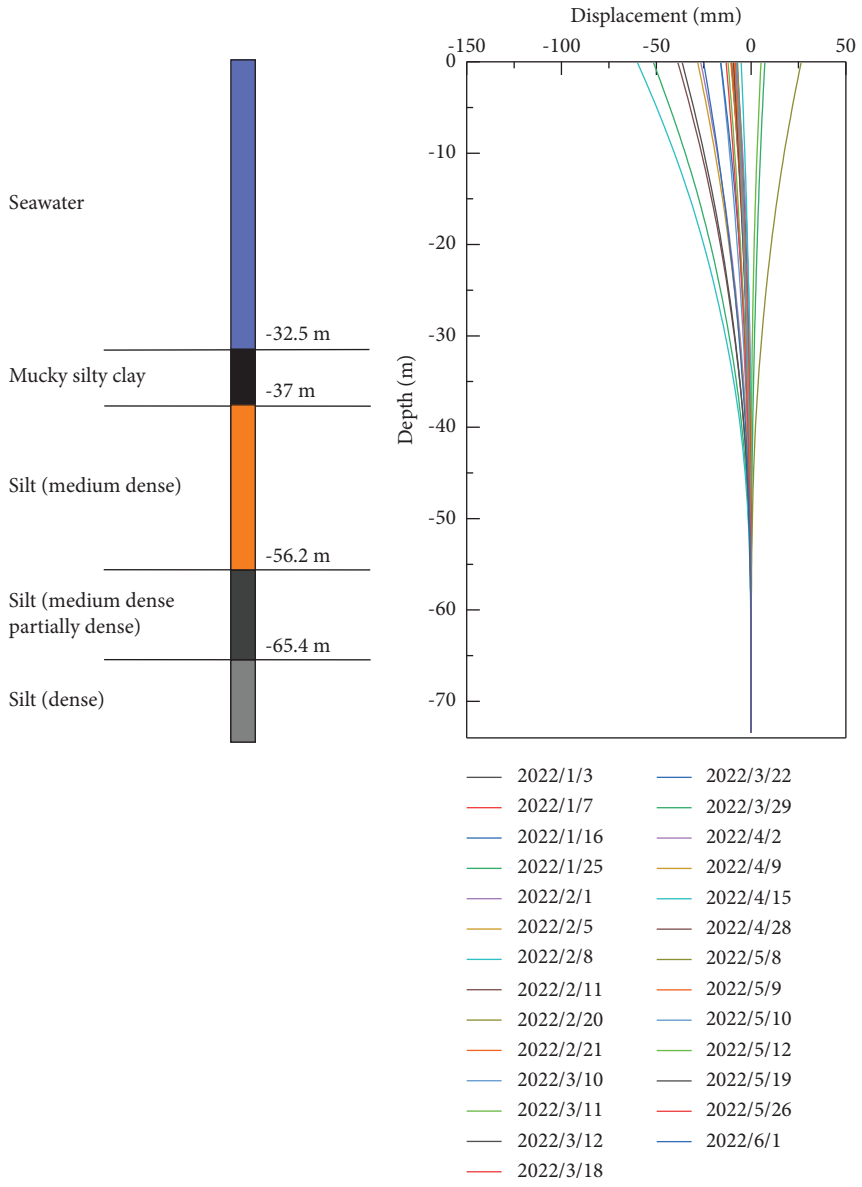

Figure 17: Horizontal displacement variation with depth of A41 pile.

threshold, the monitoring system will issue a level I warning, predicting that the wind farm may be in a bad operating environment and should be observed continuously for a while to determine whether it reaches the SLS. If the rotation angle frequently exceeds the safety threshold with an increasing tendency, the system will determine that the wind power base reaches the SLS and gives a level II warning. At the same time, the wind turbine will not work properly.

Taking the A41 wind power foundation as an example, the real-time monitoring data from January 1, 2022, to June 1, 2022 (Figure 20) showed that during this period, the mud surface rotational angle did not exceed the safety threshold, and the maximum value was 0.246 at 15:00 on February 1, without triggering an early warning. The system automatically reported that the wind turbine was in a normal operation state.

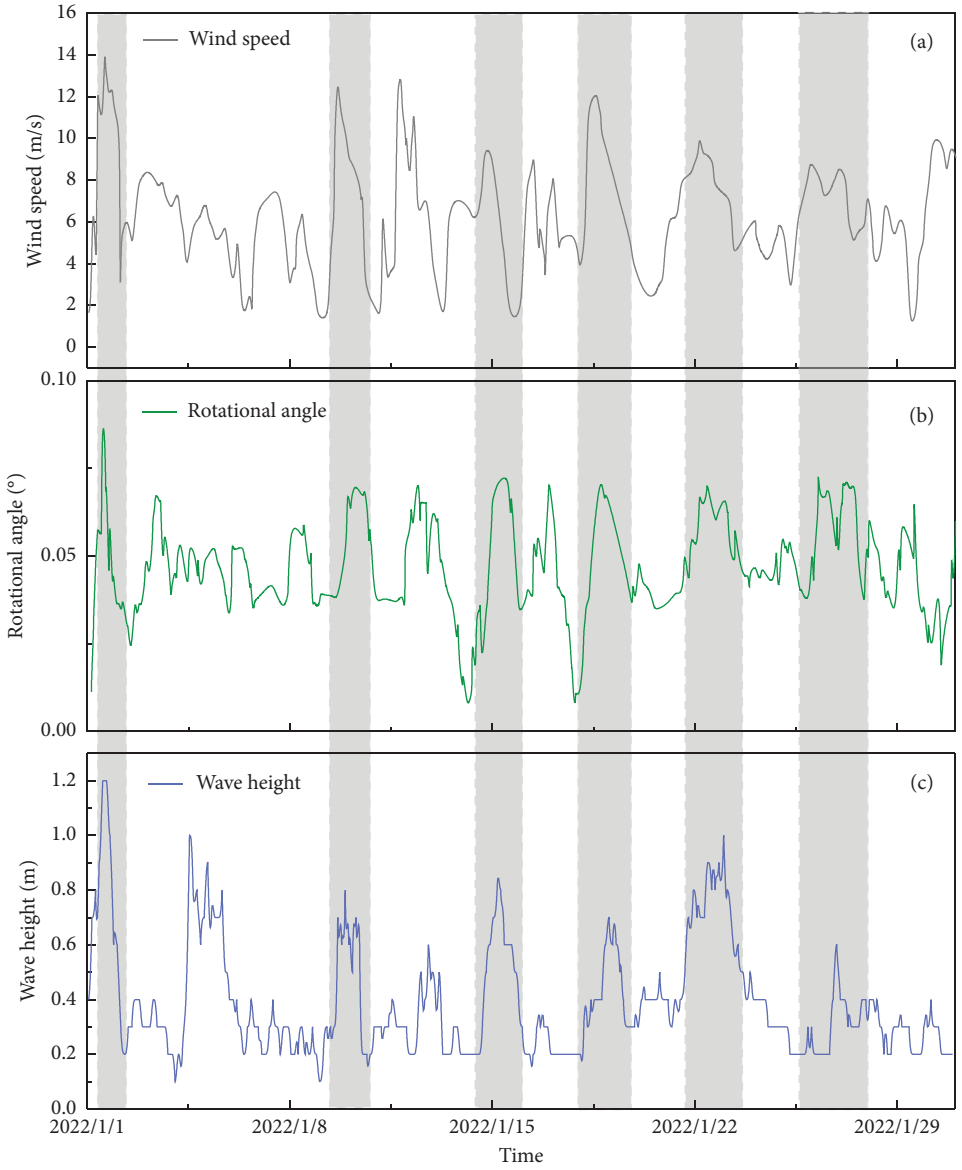

Figure 18: The curve of the pile tilt angle changing with wind speed and wave height.

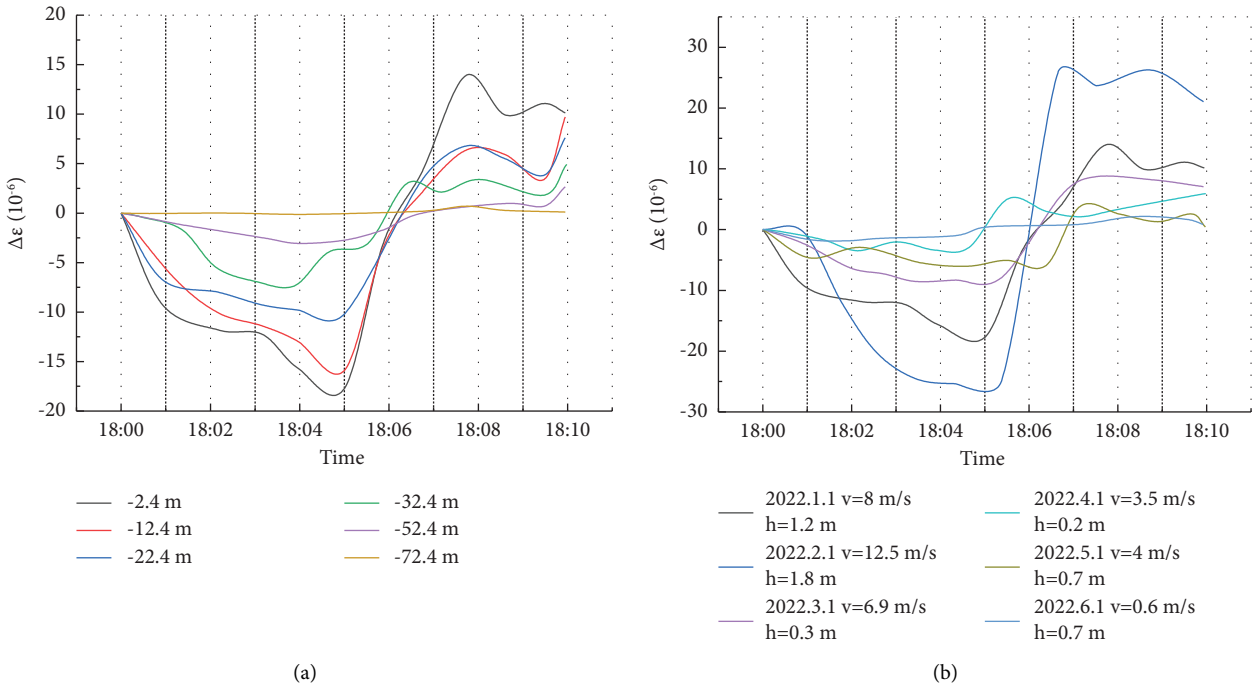

Figure 19: Variation curves of pile strain at different depths (a) and (b) seasons.

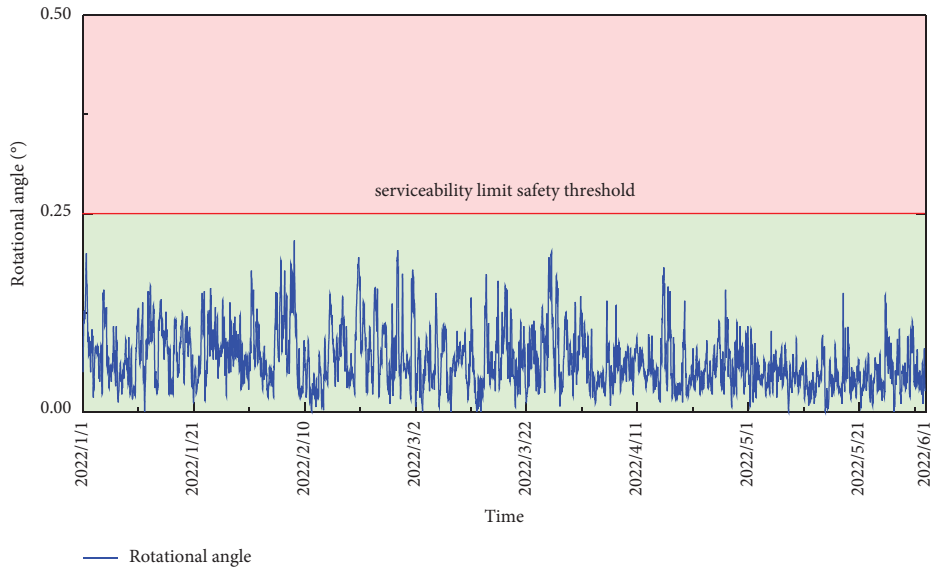

Figure 20: Wind power infrastructure health monitoring and early warning system.

5. Conclusions

Based on UWFBGs, a wireless sensor network for offshore steel pipe pile monitoring was proposed, and a case study in South Shandong Peninsula, China was demonstrated. UWFBGs were adopted to automatically obtain the pile strain during the static load test as well as the operation period to achieve life cycle monitoring. For the offshore steel pipe pile, the load transfer behavior was analyzed and the working state was evaluated. The following conclusions can be drawn:

(1) The UWFBG-based wireless sensor network used for offshore steel pipe pile monitoring is first proposed, which is efficient in mapping the distributed strain along the pile and realizes the remote sensing for life cycle monitoring of offshore steel pipe piles.

(2) Under the vertical static load, the vertical strain of the pile increases with the load and decreases with the depth. The internal force distribution of the offshore steel pipe pile is closely related to the property of the soil around the pile, and the

maximum shaft friction is located at the layer with the highest density. In addition, the tip resistance only bores 16.89% indicating that the test pile should be defined as an end-bearing friction pile.

(3) Under the horizontal static load, with an increase in depth, the strain increases first and then decreases, the peak of pile bending moment transfers to the deeper layer, and the horizontal displacement gradually decreases. The calculated displacement is compared with the measured data by using dial indicators, and the MAPE value is only 0.058, proving accurate and credible monitoring.

(4) During operation time, the strain data obtained from the Shandong Peninsula offshore wind power project reflect the sea level and water-mud interface and show that the maximum displacement occurs at the uppermost end of the fiber with an absolute value of 75 mm.

(5) The horizontal deformation of the wind turbine pile is positively correlated with the wind, wave, and current load and decreases with an increase of depth. Half-year monitoring results show that the horizontal deformation in winter is significantly greater than that in other seasons owing to the seasonal ocean current.

(6) The UWFBG-based fiber-optic wireless sensor network can be used for early warning of offshore wind piles. Setting 0.25° for the rotational angle of the mud surface as a serviceability limit safety threshold, the wind turbine in the study area is in a normal operation state.

The field study presented in this paper will provide a valuable reference for performance monitoring and evaluation of steel pipe piles, especially offshore overlength ones. Certainly, longer monitoring data will provide a more comprehensive basis for analysis.

Data Availability

The data that support the findings of this study are available on request from the corresponding author.

Conflicts of Interest

The authors declare that they have no conflicts of interest.

Acknowledgments

The authors gratefully acknowledge the financial support provided by the National Natural Science Foundation of China (Grant no. 41907232). The authors would like to extend their appreciation to Suzhou NanZee Sensing Technology Co., Ltd. for their valuable help and support in the study.

References

[1] Y. Q. Xiao and X. J. Jia, "Development status and technology analysis of offshore wind power in China," *East China Electric Power*, vol. 38, no. 2, pp. 277–280, 2010.

[2] X. J. Sun, D. G. Huang, and G. Q. Wu, "The current state of offshore wind energy technology development," *Energy*, vol. 41, no. 1, pp. 298–312, 2012.

[3] C. Sun, J. Chen, and Z. Tang, "New energy wind power development status and future trends," in *Proceedings of the 2021 International Conference on Advanced Electrical Equipment and Reliable Operation (AEERO)*, pp. 1–5, Beijing, China, October 2021.

[4] C. J. Liu, "Pile testing of large steel pile of yangshan port study on bearing capacity of large steel pile," MA thesis, Tsinghua University, Tsinghua China, 2009.

[5] S. Bhattacharya, T. Carrington, and T. Aldridge, "Observed increases in offshore pile driving resistance," *Proceedings of the Institution of Civil Engineers-Geotechnical Engineering*, vol. 162, no. 1, pp. 71–80, 2009.

[6] C. Baldwin, T. Poloso, P. C. Chen, J. B. Niemczuk, and C. Ealy, "Structural monitoring of composite marine piles using fiber optic sensors," in *Proceedings of the SPIE International Society for Optical Engineering*, March 2001, Newport Beach, CF, USA.

[7] S. J. Feng, S. F. Lu, and Z. M. Shi, "Field investigations of two super-long steel pipe piles in offshore areas," *Marine Georesources & Geotechnology*, vol. 34, no. 6, pp. 559–570, 2015.

[8] B. H. Fellenius, D. E. Harris, and D. G. Anderson, "Static loading test on a 45 m long pipe pile in Sandpoint, Idaho," *Canadian Geotechnical Journal*, vol. 41, no. 4, pp. 613–628, 2004.

[9] L. J. Huang, Y. Lin, J. Cai, and W. Q. Zhou, "Dynamic and static comparative analyses of settlements of overlength PHC pipe piles," *Rock and Soil Mechanics*, vol. 29, no. 2, pp. 507–511, 2008.

[10] H. Seo, M. Prezzi, and R. Salgado, "Instrumented static load test on rock-socketed micropile," *Journal of Geotechnical and Geoenvironmental Engineering*, vol. 139, no. 12, pp. 2037–2047, 2013.

[11] A. Leal-Junior, J. Casas, C. Marques, M. J. Pontes, and A. Frizera, "Application of additive layer manufacturing technique on the development of high sensitive fiber Bragg grating temperature sensors," *Sensors*, vol. 18, no. 12, p. 4120, 2018.

[12] X. Qiao, Z. Shao, W. Bao, and Q. Rong, "Fiber bragg grating sensors for the oil industry," *Sensors*, vol. 17, 2017.

[13] D. Kinet, P. Mégret, K. Goossen, L. Qiu, D. Heider, and C. Caucheteur, "Fiber Bragg grating sensors toward structural health monitoring in composite materials: challenges and solutions," *Sensors*, vol. 14, no. 4, pp. 7394–7419, 2014.

[14] T. Guo, F. Liu, B. Guan, and J. Albert, "Tilted fiber grating mechanical and biochemical sensors," *Optics & Laser Technology*, vol. 78, pp. 19–33, 2016.

[15] V. Mishra, N. Singh, U. Tiwari, and P. Kapur, "Fiber grating sensors in medicine: current and emerging applications," *Sensors and Actuators A: Physical*, vol. 167, no. 2, pp. 279–290, 2011.

[16] C. Markos, A. Stefani, K. Nielsen, H. K. Rasmussen, W. Yuan, and O. Bang, "High-T_g TOPAS microstructured polymer optical fiber for fiber Bragg grating strain sensing at 110 degrees," *Optics Express*, vol. 21, no. 4, pp. 4758–4765, 2013.

[17] W. Zhang, D. J. Webb, and G. D. Peng, "Enhancing the sensitivity of poly(methyl methacrylate) based optical fiber Bragg grating temperature sensors," *Optics Letters*, vol. 40, no. 17, p. 4046, 2015.

[18] R. Ishikawa, H. Lee, A. Lacraz et al., "Pressure dependence of fiber Bragg grating inscribed in perfluorinated polymer fiber," *IEEE Photonics Technology Letters*, vol. 29, no. 24, pp. 2167–2170, 2017.

[19] A. Leal-Junior, J. J. Guo, R. Min, A. J. Fernandes, A. Frizera, and C. Marques, "Photonic smart bandage for wound healing assessment," *Photonics Research*, vol. 9, no. 3, pp. 272–280, 2021.

[20] D. P. Kong, D. M. Zhang, Y. Yuan et al., "Progress in research and applications of plastic optica fiber," *Acta Photonica Sinica*, vol. 48, no. 11, 2019.

[21] X. Yao, "Discussion on optical fiber communication technology and optical fiber transmission system," *Telecom World*, vol. 26, no. 5, pp. 139-140, 2019.

[22] Q. Xu, Y. Zhao, W. L. Luo, C. Chen, S. B. Lin, and Y. N. Zhang, "Characteristics of terahertz waveguide based on cyclic olefin copolymer photonic crystal fiber," *Laser Journal*, vol. 40, no. 1, pp. 83–86, 2019.

[23] L. Zhang, H. H. Zhu, H. M. Han, and B. Shi, "Fiber optic monitoring of an anti-slide pile in a retrogressive landslide," *Journal of Rock Mechanics and Geotechnical Engineering*, 2023.

[24] L. Zhang, Y. F. Cui, H. H. Zhu et al., "Shear deformation calculation of landslide using distributed strain sensing technology considering the coupling effect," *Landslides*, 2023.

[25] H. Mohamad, K. Soga, and B. Amatya, "Thermal strain sensing of concrete piles using Brillouin optical time domain reflectometry," *Geotechnical Testing Journal*, vol. 37, no. 2, Article ID 20120176, 2014.

[26] L. Pelecanos, K. Soga, M. P. Chunge et al., "Distributed fibre optic monitoring of an osterberg-cell pile test in london," *Géotechnique Letters*, vol. 7, no. 2, pp. 152–160, 2017.

[27] L. Pelecanos, K. Soga, M. Z. E. B. Elshafie et al., "Distributed fiber optic sensing of axially loaded bored piles," *Journal of Geotechnical and Geoenvironmental Engineering*, vol. 144, no. 3, Article ID 04017122, 2018.

[28] B. Shi, D. Zhang, and H. H. Zhu, *Distributed Fiber Optic Sensing for Geoengineering Monitoring*, Science Press, Beijing, China, 2019.

[29] W. R. Habel, K. Krebber, and K. Krebber, "Fiber-optic sensor applications in civil and geotechnical engineering," *Photonic Sensors*, vol. 1, no. 3, pp. 268–280, 2011.

[30] C. S. Kim, T. H. Lee, Y. S. Yu, Y. G. Han, S. B. Lee, and M. Y. Jeong, "Multi-point interrogation of FBG sensors using cascaded flexible wavelength-division Sagnac loop filters," *Optics Express*, vol. 14, no. 19, pp. 8546–8551, 2006.

[31] G. Gagliardi, M. Salza, P. Ferraro, and P. De Natale, "Fiber Bragg-grating strain sensor interrogation using laser radio-frequency modulation," *Optics Express*, vol. 13, no. 7, pp. 2377–2384, 2005.

[32] C. C. Chan, W. Jin, D. N. Wang, and M. S. Demokan, "Intrinsic crosstalk analysis of a serial TDM FGB sensor array by using a tunable laser," *Microwave and Optical Technology Letters*, vol. 36, no. 1, pp. 2–4, 2003.

[33] J. H. He, J. C. Zhang, Y. Chen et al., "Automatic land subsidence monitoring system based on weak-reflection fiber gratings," *Hydrogeology & Engineering Geology*, vol. 48, no. 1, pp. 146–153, 2021.

[34] H. Y. Guo, J. G. Tang, X. F. Li, Y. Zheng, and H. F. Yu, "Online writing weak fiber Bragg gratings array," *Chinese Optics Letters*, vol. 11, no. 3, Article ID 030602, 2013.

[35] Y. Muanenda, S. Faralli, C. J. Oton, C. Cheng, M. Yang, and F. Di Pasquale, "Dynamic phase extraction in high-SNR DAS based on UWFBGs without phase unwrapping using scalable homodyne demodulation in direct detection," *Optics Express*, vol. 27, no. 8, pp. 10644–10658, 2019.

[36] Y. Wang, J. Gong, D. Y. Wang, B. Dong, W. Bi, and A. Wang, "A quasi-distributed sensing network with time-division-multiplexed fiber Bragg gratings," *IEEE Photonics Technology Letters*, vol. 23, no. 2, pp. 70–72, 2011.

[37] M. L. Zhang, Q. Z. Sun, Z. Wang, X. L. Li, H. R. Liu, and D. M. Liu, "Investigation on distributed optical fiber sensor based on identical-low-reflective fiber gratings," *Laser Optoelectronics Progress*, vol. 48, no. 8, Article ID 80604, 2011.

[38] P. Moyo, J. M. W. Brownjohn, R. Suresh, and S. C. Tjin, "Development of fiber Bragg grating sensors for monitoring civil infrastructure," *Engineering Structures*, vol. 27, no. 12, pp. 1828–1834, 2005.

[39] J. P. Jiang, W. B. Gan, Y. Hu et al., "Real-time monitoring method for unauthorized working activities above the subway tunnel based on ultra-weak fiber Bragg grating vibration sensing array," *Measurement*, vol. 182, Article ID 109744, 2021.

[40] H. Liu Sheng, Y. Han Xinying, C. Xiong Yuchuan, and W. Wen Hongqiao, "Distributed vibration detection system based on weak fiber Bragg grating array," *Chinese Journal of Lasers*, vol. 44, no. 2, Article ID 0210001, 2017.

[41] Z. H. Zhang, P. Guan, J. L. Xu, B. Z. Wang, H. Li, and Y. K. Dong, "Horizontal loading performance of offshore wind turbine pile foundation based on DPP-BOTDA," *Applied Sciences*, vol. 10, no. 2, pp. 492–756, 2020.

[42] J. D. Qiu, J. Liu, X. H. Kong et al., "Marine geo-hazards in the coastal and offshore area of southern Shandong Peninsula," *Marine Geology & Quaternary Geology*, vol. 32, no. 1, pp. 27–34, 2012.

[43] J. R. Cui and D. X. Xia, "The relationship between coastal morphology and the characteristics of waves and tides of Shandong Peninsula," *J. Oceanography of Huanghai and Bohai seas*, vol. 10, no. 3, pp. 20–25, 1992.

[44] DNV, "Design of floating wind turbine structures," 2013, https://www.dnv.com/energy/standards-guidelines/dnv-st-0119-floating-wind-turbine-structures.html.

[45] L. Arany, S. Bhattacharya, J. H. G. Macdonald, and S. J. Hogan, "A critical review of serviceability limit state requirements for monopile foundations of offshore wind turbines," in *Proceedings of the Offshore Technology Conference*, Houston, Texas, USA, May 2015.

[46] DNV, "Support structures for wind turbines," 2021, https://www.dnv.com/energy/standards-guidelines/dnv-st-0126-support-structures-for-wind-turbines.html.